

Combining Machine Learning with Recurrence Analysis for resonance detection

Ondřej Zelenka ^{1,*} Ondřej Kopáček ^{1,2} and Georgios Lukes-Gerakopoulos ¹

¹*Astronomical Institute of the Czech Academy of Sciences,
Boční II 1401/1a, CZ-141 00 Prague, Czech Republic*

²*Faculty of Science, Humanities and Education, Technical University of Liberec,
Studentská 1402/2, CZ-461 17 Liberec, Czech Republic*

(Dated: December 30, 2024)

The width of a resonance in a nearly integrable system, i.e. in a non-integrable system where chaotic motion is still not prominent, can tell us how a perturbation parameter is driving the system away from integrability. Although the tool that we are presenting here can be used is quite generic and can be used in a variety of systems, our particular interest lies in binary compact object systems known as extreme mass ratio inspirals (EMRIs). In an EMRI a lighter compact object, like a black hole or a neutron star, inspirals into a supermassive black hole due to gravitational radiation reaction. During this inspiral the lighter object crosses resonances, which are still not very well modeled. Measuring the width of resonances in EMRI models allows us to estimate the importance of each perturbation parameter able to drive the system away from resonances and decide whether its impact should be included in EMRI waveform modeling or not. To tackle this issue in our study we show first that recurrence quantifiers of orbits carry imprints of resonant behavior, regardless of the system's dimensionality. As a next step, we apply a long short-term memory machine learning architecture to automate the resonance detection procedure. Our analysis is developed on a simple standard map and gradually we extend it to more complicated systems until finally we employ it in a generic deformed Kerr spacetime known in the literature as the Johannsen-Psaltis spacetime.

I. INTRODUCTION

Nonintegrable dynamical systems exhibit a high level of complexity in their dynamics due to the absence of sufficient conserved quantities (integrals of motion). Unlike a completely integrable system in which the number of integrals matches the degrees of freedom and the dynamics is always *regular* (and thus predictable), a nonintegrable system, in general, allows for chaotic dynamics, which makes long-term predictability impossible [1]. Nevertheless, in the weakly nonintegrable system, deterministic chaos is typically not a prominent feature, and chaotic layers in its phase space are rather thin (i.e., the phase space is still dominated by regular dynamics). Instead, the most relevant hallmark of nonintegrability in a weakly nonintegrable system is the presence of so-called Birkhoff chains, which reflect the increasing width of resonances [2].

The width of a resonance generally grows with the strength of (still weak) nonintegrable perturbation parameter [3] and, especially for the most prominent resonances characterized by frequency ratios given by small integers (e.g., 1:2 or 2:3 resonances), it may grow to a significant size and occupy a considerable portion of the phase space. Therefore, these resonances may become an important factor affecting the overall dynamics of the system and must be taken into account in the analysis of trajectories that may approach the resonant region of associated Birkhoff islands of stability.

The investigation of resonant features in weakly non-integrable dynamical systems is important for a wide

range of disciplines, including various branches of fundamental and applied research and engineering. Our motivation comes from the field of relativistic astrophysics. In particular, we investigate a dynamical system consisting of a smaller body orbiting a much more massive rotating black hole. An astrophysical system of this type is not perfectly conservative, and the energy and the angular momentum of the orbiting body are slowly decreasing and radiated away in the form of gravitational waves; the orbit gradually shrinks and the system is actually evolving as an Extreme Mass Ratio Inspiral (EMRI) [4]. Gravitational waves emitted by EMRIs will be detectable by future gravitational observatories (e.g., LISA [5]).

Nevertheless, the complete integrability of the EMRI system is only guaranteed as far as the idealization of the orbiting point mass is concerned. This is hardly the case, and integrability will be inevitably perturbed to some degree, and Birkhoff chains will grow in the phase space. The question arises whether and how such prolonged resonances induced by nonintegrable perturbations [6] (caused, e.g., by the presence of extra matter around the central object [7] or by finite size and rotation of the smaller body [8]) may affect emitted gravitational waveforms and detectability of EMRIs modeled as systems with three or more non-reducible degrees of freedom.

To this end, we first develop a robust and generally applicable technique for the detection of resonances in the phase space of a (weakly) nonintegrable dynamical system with an arbitrary number of degrees of freedom. Our method combines the benefits of recurrence analysis [9] with the machine learning approach. In the current paper, we first describe the method and demonstrate its abilities on simple systems (standard and de Voge-

* ondrej.zelenka@asu.cas.cz

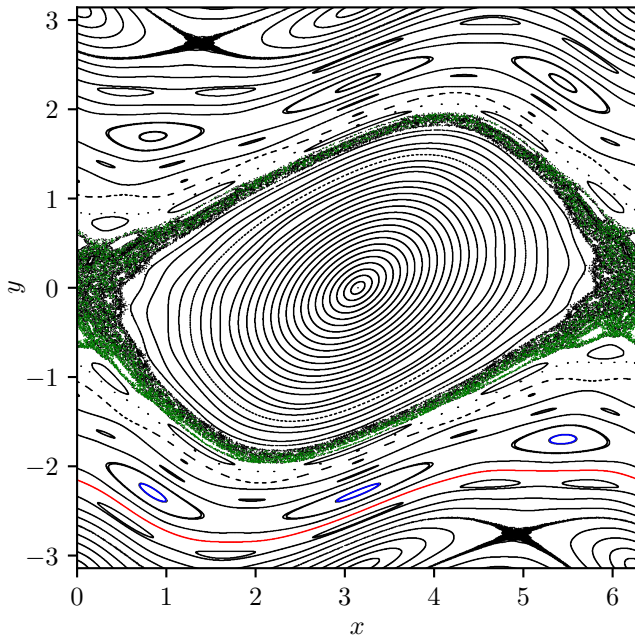


Figure 1. Phase portrait of the standard map (see Eqs. 14) with $K = 0.8$, showing the standard hallmarks of chaotic maps: KAM curves, Birkhoff chains, and chaotic layers. The regular, resonant, and chaotic orbits which produce the recurrence plots of Fig. 2 are highlighted in red, blue, and green, respectively.

leare maps). Then we shift to a 4D map, to show that our method works on higher dimensional systems. Finally, we employ our method on a generically deformed Kerr black hole spacetime [10] as an application on the astrophysical problem of EMRIs.

The rest of the article is organized as follows. Our experimental setup is provided in Sec. II, in which we brief an introduction into dynamical systems, recurrence analysis, embedding, the employed machine learning architecture and its training. Sec. III presents our obtained results from the machine learning method we employed. Our conclusions are given in Sec. IV.

II. EXPERIMENTAL SETUP

A. Dynamical systems

1. Hamiltonian systems

Many systems in physics can be written in the form of a Hamiltonian system. With d degrees of freedom, it consists of

- generalized coordinates q^i , $i = 1, \dots, d$,
- canonical momenta p_i , $i = 1, \dots, d$,
- a Hamiltonian function $H(q^i, p_i)$.

The equations of motion then have the form

$$\frac{dq^i}{dt} = \frac{\partial H}{\partial p_i}, \quad (1a)$$

$$\frac{dp_i}{dt} = -\frac{\partial H}{\partial q^i}. \quad (1b)$$

In such a system it holds that the Hamiltonian H is itself an integral of motion.

A special case is a so-called *integrable* system. When d linearly independent conserved quantities F_1, \dots, F_d in involution

$$\frac{dF_i}{dt} = 0, \quad \sum_{k=1}^d \left(\frac{\partial F_i}{\partial q^k} \frac{\partial F_j}{\partial p_k} - \frac{\partial F_i}{\partial p_k} \frac{\partial F_j}{\partial q^k} \right) = 0. \quad (2)$$

exist, there exists a set of *action-angle coordinates* θ^i , ω_i such that

$$\frac{d\theta^i}{dt} = \omega_i, \quad \frac{d\omega_i}{dt} = 0. \quad (3)$$

The motion then takes place on a set of invariant tori which foliate the entire phase space. The actions ω_i correspond to *fundamental frequencies* of the individual degrees of freedom. A torus whose fundamental frequencies are commensurable (i.e. their ratio is a rational number) consists of periodic orbits and is called *resonant*.

The application of a small perturbation transforms the phase space into a *near-integrable* system, which follows two elementary theorems:

- the Kolmogorov-Arnold-Moser theorem [11–13]: some of the non-resonant tori survive deformed,
- the Poincaré-Birkhoff theorem [14]: the resonances form thinner tori which cross the surface of section multiple times before connecting back to the initial circle, surrounded by a thin chaotic zone.

2. Dynamical maps

The structure of a $d = 2$ Hamiltonian system's phase space is commonly visualized using a *Poincaré section*. A surface of section is defined in the phase space such that the Hamiltonian flow is not tangent at any point of the surface, and successive intersections of the orbit and the surface of section are recorded and form the Poincaré section. The mapping of an initial condition on the surface of section to the next intersection is called the return mapping.

In an integrable system, all successive interactions of an orbit with the surface of section lie on the intersection of the corresponding invariant torus with the surface of section, which is topologically a circle. In the case of a resonant torus, the intersections form isolated points, while a quasiperiodic torus produces gradually fills the circle densely.

The typical behavior of return mappings of near-integrable systems, such as a main island of stability containing chaotic layers and Birkhoff chains surrounded by a chaotic sea, can be observed in general dynamical maps.

This includes the return mapping of a Hamiltonian system, which is thus also a dynamical map.

B. Recurrence analysis

Recurrence analysis is based on systematic observations of a dynamical system visiting a similar state repeatedly. The recurrence plot (RP) of a system is based on the recurrence matrix [9]

$$\mathbf{R}_{i,j} = \begin{cases} 1 & : |\vec{x}_i - \vec{x}_j| \leq \epsilon, \\ 0 & : |\vec{x}_i - \vec{x}_j| > \epsilon, \end{cases} \quad i, j = 1, \dots, N, \quad (4)$$

Clearly, the main diagonal is filled with ones, as $\forall i |\vec{x}_i - \vec{x}_i| = 0$. This is a structure which is undesirable for some of the further steps, therefore a *Theiler window* is applied, which zeros out all elements on the

main diagonal. Optionally, this can apply to elements up to a fixed distance from the main diagonal; however, this is a feature not used in this paper.

A visualization of the recurrence matrix using black/white dots for the 1/0 values is called a RP. Provided a suitable choice of parameters, it can reveal many properties of a dynamical system: a quasiperiodic orbit forms diagonal lines that are offset from each other by the time the system takes to return to an ϵ distance from a previous state as seen in the left panel of Fig. 2. A chaotic orbit, on the other hand, forms structures that are generally less organized but resemble those of a quasiperiodic orbit when in a sticky zone. These manifest themselves as separated squares along the main diagonal, see the right panel of Fig. 2.

Besides visual survey of RPs, one can also perform recurrence quantification analysis (RQA) and employ the recurrence matrix $\mathbf{R}_{i,j}$ to calculate various statistical measures related to characteristic structures appearing in RPs. In particular, we make use of the RQA measures based on the distributions of diagonal lines of length l , $P(\epsilon, l)$, and vertical lines of length v , $P(\epsilon, v)$ which are defined as follows:

$$P(\epsilon, l) = \sum_{i,j=1}^N (1 - \mathbf{R}_{i-1,j-1}(\epsilon)) (1 - \mathbf{R}_{i+l,j+l}(\epsilon)) \prod_{k=0}^{l-1} \mathbf{R}_{i+k,j+k}(\epsilon), \quad (5a)$$

$$P(\epsilon, v) = \sum_{i,j=1}^N (1 - \mathbf{R}_{i,j}(\epsilon)) (1 - \mathbf{R}_{i,j+v}(\epsilon)) \prod_{k=0}^{v-1} \mathbf{R}_{i,j+k}. \quad (5b)$$

First of all, the recurrence rate RR is calculated to measure the relative number of recurrences (i.e., the average density of black dots in the respective RP):

$$\text{RR} = \frac{1}{N^2} \sum_{i,j=1}^N \mathbf{R}_{i,j}(\epsilon). \quad (6)$$

The value of RR has an obvious dependence on threshold ϵ . Higher ϵ means more recurrences and higher RR. In some applications, it appears useful to use the fixed recurrence rate option, i.e., to first specify the value of RR and find the corresponding ϵ , which is then used to calculate other RQA measures and to construct the RP.

In our analysis we employ the following RQA indicators based on the distribution of diagonal lines:

- determinism

$$\text{DET} = \frac{\sum_{l=l_{\min}}^N lP(l)}{\sum_{l=1}^N lP(l)}, \quad (7)$$

- average diagonal line length (of minimal length

l_{\min})

$$L = \frac{\sum_{l=l_{\min}}^N lP(l)}{\sum_{l=l_{\min}}^N P(l)}, \quad (8)$$

- longest diagonal line and divergence

$$L_{\max} = \max(\{l_i\}_{i=1}^{N_i}), \quad \text{DIV} = \frac{1}{L_{\max}}, \quad (9)$$

- entropy of the diagonal line distribution

$$L_{\text{entr}} = - \sum_{l=l_{\min}}^N P(l) \log P(l), \quad (10)$$

and the following RQA measures based on the distribution of vertical lines:

- laminarity

$$\text{LAM} = \frac{\sum_{v=v_{\min}}^N vP(v)}{\sum_{v=1}^N vP(v)}, \quad (11)$$

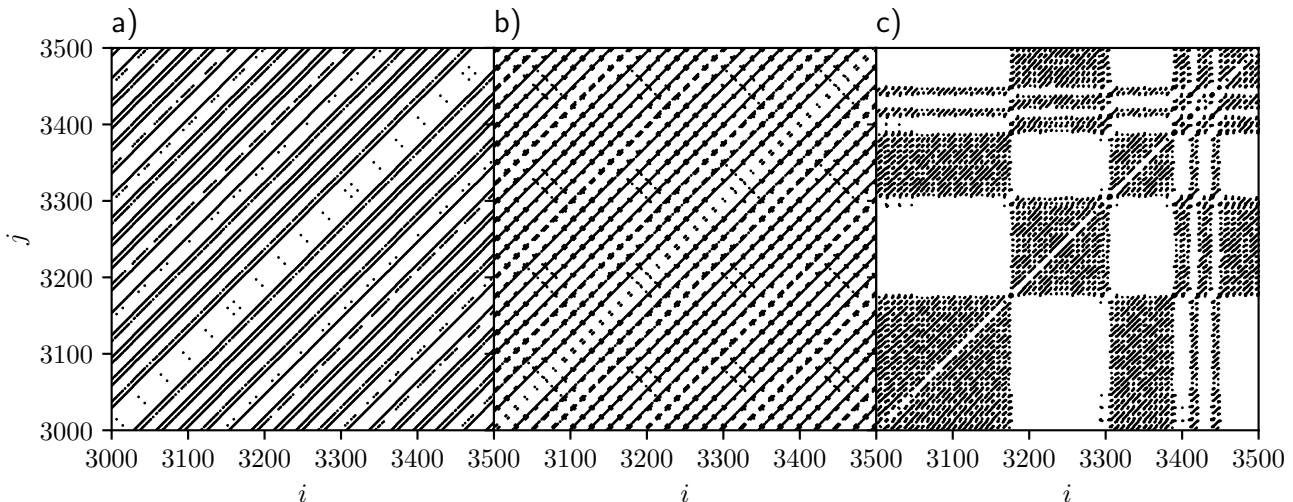


Figure 2. Examples of recurrence plots of trajectories of the standard map with $K = 0.8$. Different recurrence thresholds are used in order to achieve a fixed $RR = 0.05$, and all three are generated using the Euclidean metric. a) KAM trajectory starting at $(x_0, y_0) = (\pi, -4\pi/5)$, using $\epsilon = 0.16471$. b) Resonant trajectory starting at $(x_0, y_0) = (\pi, -37\pi/50)$, using $\epsilon = 0.045881$. c) Chaotic trajectory starting at $(x_0, y_0) = (\pi, -27\pi/50)$, using $\epsilon = 0.286985$.

- and the longest vertical line

$$V_{\max} = \max \left(\{v_l\}_{l=1}^{N_v} \right). \quad (12)$$

The explicit dependence of the above indicators on threshold ϵ is not stressed anymore for the brevity. The values of l_{\min} and v_{\min} are independent parameters which specify the lengths of the shortest diagonal and vertical lines considered for the analysis. Both values are set to 2 by default. For more details and definitions of another RQA measures, we refer to [9].

The RQA quantifiers encode many dynamical properties of the underlying system, such as the correlation entropy and dimension, or the maximum Lyapunov exponent [9]. Nevertheless, the relations between these dynamical invariants and RQA measures are not straightforward due to their dependence on parameters of the recurrence analysis [15]. In particular, RQA quantifiers do not directly recognize whether the trajectory is resonant (i.e., belonging to the particular Birkhoff chain) or nonresonant (i.e., represented by a KAM curve in the two-dimensional phase portrait).

Recurrence analysis proved very useful in analyses of strongly nonintegrable systems [16, 17] in which the Birkhoff chains are typically surrounded by prominent chaotic regions ("islands of stability in the chaotic sea"). In such a case, the detection and localization of the resonant region in the phase space is based on the distinction between chaotic and resonant quasiperiodic orbits. For this task, the recurrence analysis appeared very effective, allowing us to distinguish between both dynamic regimes on a shorter time scale compared to standard tools like Lyapunov characteristic exponents.

Nevertheless, in a weakly nonintegrable system, the problem becomes more subtle as the Birkhoff chains

are typically surrounded by KAM tori of (nonresonant) quasiperiodic orbits (very thin chaotic layers are not relevant in this context). In order to localize the resonance, we, therefore, need to unambiguously distinguish between the regular quasiperiodic orbits belonging to the resonance and nearby KAM tori. In a system of two degrees of freedom, the method of choice for this specific task would be a rotation number, which is directly related to the characteristic frequency ratios of the orbits. However, for the system of three or more degrees of freedom, the rotation number (computed from the Poincaré surface of section) has not been defined yet, and more general methods need to be applied. We propose employing recurrence analysis, which is applicable regardless of the number of degrees of freedom. On the other hand, the relations of RQA measures to frequencies of the orbit are not direct, and they are further obscured by dependence on the parameters of the recurrence analysis (in particular, the threshold ϵ).

However, as one can observe in Fig. 3 which shows the dependence of several RQA measures on initial conditions of trajectories for several values of ϵ , the resonances clearly do affect the values of recurrence quantifiers, and their behaviour thus in principle allows to distinguish between resonant and nonresonant orbits and measure the width of the resonance. Nevertheless, unlike rotation numbers which remain constant within resonances and allow to detect resonances easily as plateaus in respective rotation curves, the interpretation of RQA curves is more complicated. In particular, the values of RQA parameters are not constant within the resonance, and their behavior depends critically on the threshold ϵ whose optimal value is not known a priori.

For example, the recurrence rate values in the top

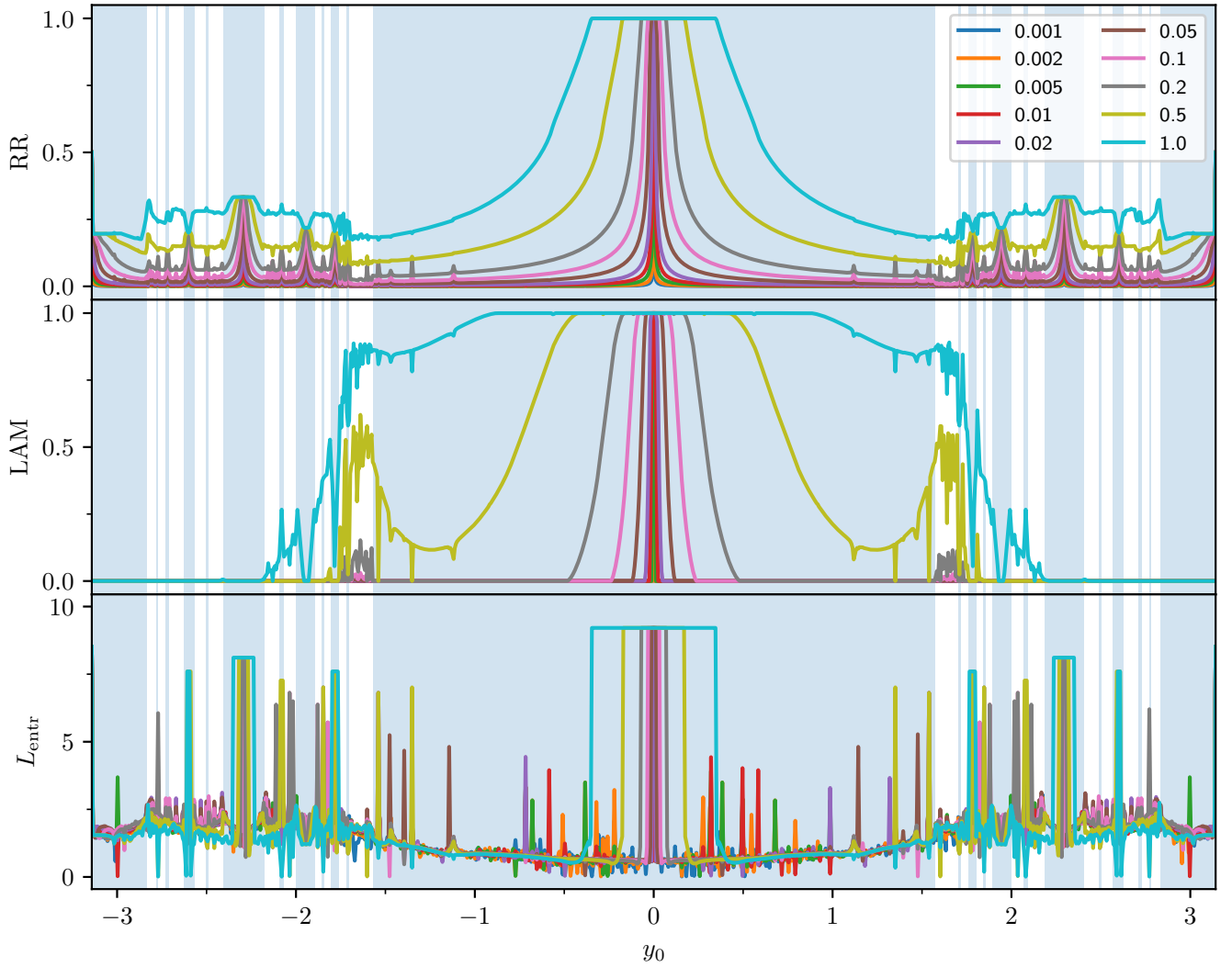


Figure 3. Example of RQA curves of the standard map at $K = 0.8$ as a function of the initial condition taken along the y -axis of Fig. 1 with $x_0 = 0$. Each of the three panel corresponds to one of the recurrence quantifiers: the recurrence rate, the laminarity, and the entropy of the diagonal lines distribution, in Eqs. (6), (11), (10), respectively. The color-coding corresponds to different recurrence thresholds given in the legend. The pale blue areas in the background show the locations of resonances as marked during the training data labeling procedure.

panel of Fig. 3 clearly respond to resonances; however, while they show peaks in most cases, the values in the resonance at approximately $y_0 \in [-2, -1.9]$ follow this behavior for most thresholds but the opposite is true for the curve with recurrence threshold $\epsilon = 1$. Thus, one should always take into account ensembles of many RQA curves with different values of ϵ covering a sufficiently wide range of recurrence rates ($\approx 1 - 20\%$). Moreover, in order to fully exploit the potential of recurrence analysis, we want to gather and combine information from the behavior of several RQA measures. In order to achieve this, we propose to employ machine learning (ML) methods.

C. Embedding

Recurrence analysis as described above relies on our knowledge of all components of the state vector. When applied to data where this is not true, such as observations of radiation from a complex source, spurious correlations pollute the recurrence matrix and reduce the faithfulness of the analysis.

To mitigate this issue, phase space reconstruction is necessary. The most common way to do this is to apply time delay embedding [9, 18], which replaces the unknown components out of time delayed elements of the known data. For simplicity, let us assume the known data to consist of a single element u_i at any given discrete time i . Then the reconstructed phase space vector

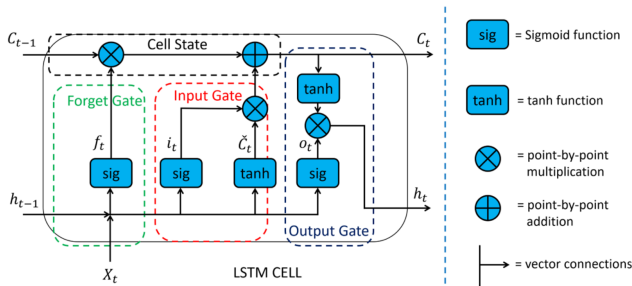


Figure 4. LSTM network architecture. Taken from [20].

is defined as

$$\vec{x}_i = \left(u_{i+(j-1)\tau} \right)_{j=1}^m, \quad (13)$$

where m and τ are parameters called the embedding dimension and time delay, respectively.

This method of phase space reconstruction is known to faithfully reproduce the full dynamics of the system. In fact, it has been proven that there exists a diffeomorphism between the original and reconstructed phase spaces [18].

D. Model architecture

A long short-term memory (LSTM) network is built of an arbitrary number of LSTM cells, one of which is depicted in Fig. 4. They are specifically designed to handle time-series data: X_t serves as the input and o_t as the output at time t . The individual LSTM cells communicate through the short-term memory h_t and the long-term memory C_t . For more details on LSTM architectures, see [19].

While in the original motivation the LSTM cells are stacked along the time direction of a time series, we follow a different approach: time-related properties of the system's orbits are encoded in the RQA quantifiers, and we stack the LSTM cells in the direction along which we pick initial conditions. This allows our network to accept arbitrary-length inputs and return series with the same length. Furthermore, we apply a bidirectional LSTM architecture, which employs the same type of cells as shown in Fig. 4, in two sets: one running in each direction.

The network depth is kept as a parameter which we vary to determine an optimal value. Furthermore, dropout layers are included inside the LSTM network as well as before the output layer with a variable dropout rate which is also optimized later.

To build an input data sample, let us have a sequence of N initial conditions, each producing a trajectory of a fixed length of 10000 points of a discrete-time system. The phase space is shifted and rescaled such that each dimension covers the interval $[0, 2\pi]$. For each trajectory, we compute RR, DET, LAM, L , L_{entr} , DIV, and V_{max} at the threshold values $\epsilon = 0.001, 0.002, 0.005,$

0.01, 0.02, 0.05, 0.1, 0.2, 0.5, 1. This produces a total of 70 RQA indicators for each orbit. The network accepts as its input tensors of shape $N \times 70$ and produces an output in the shape $N \times 1$, meant to correspond to the network's degree of confidence that the corresponding orbit is part of a resonant island of stability, in the range $(0, 1)$.

The network is composed of the `torch.nn.LSTM` module with input and hidden sizes set to 70, followed by a dropout layer, a fully connected layer combining its input to a single output, and finally a Sigmoid layer maps it to the interval $[0, 1]$.

Each dataset sample is a collection of these 70 recurrence quantifiers for a set of different trajectories of the system and represents a sweep of initial conditions along a line in the phase space.

E. Training and validation data

For training and validation data, we make use of a simple system typical for demonstrations of dynamical system properties. This is the Standard map [21] defined as

$$x_{n+1} = x_n + y_{n+1}, \quad (14a)$$

$$y_{n+1} = y_n + K \sin(x_n), \quad (14b)$$

with K a perturbation parameter. We have chosen the Standard map, since it is essentially a kicked pendulum and the dynamics of a pendulum essentially encapsulates the dynamics of a resonance [22]. Each dataset sample is generated for a fixed value of K using a set of 1001 equidistant initial conditions covering the interval $y \in [-\pi, \pi]$ at $x = 0$. In particular, the training dataset consists of $K = 0, 0.1, \dots, 1$, while the validation dataset $K = 0.05, 0.15, \dots, 0.95$.

The data are hand-labeled: each initial condition is assigned the value 1 if it is part of a resonant island of stability, and 0 if it is not. As the purpose of this model is to detect the resonances based on correlations between recurrence quantifiers of different initial conditions, we only mark islands as resonant if there are at least two neighboring initial conditions in the island.

F. Test data

To demonstrate the effectiveness of the trained networks, we use test data coming from three different systems with specific properties.

1. Dynamical mapping: de Voigeleare map

For the simpler test data, we use the de Voigeleare map [23], defined as

$$x_{n+1} = -y_n + Kx_n + x_n^2, \quad (15a)$$

$$y_{n+1} = x_n - Kx_{n+1} - x_{n+1}^2, \quad (15b)$$

with $K \in \mathbb{R}$ a perturbation parameter.

2. Poincaré section: motion around a black hole

One of the aims of the method developed in this paper is the search for extended resonances in the motion of a test particle around a black hole. Knowledge of their locations will allow us to properly model the qualitatively distinct behavior of the passage through these resonances.

We consider a particle moving along a geodesic in the vicinity of a perturbed black hole, which could model the evolution of an EMRI in modified gravity. The Johannsen-Psaltis spacetime is given by the line element [10, 24]

$$ds^2 = g_{tt}dt^2 + g_{rr}dr^2 + g_{\theta\theta}d\theta^2 + g_{\phi\phi}d\phi^2 + 2g_{t\phi}dtd\phi \quad (16)$$

with metric components

$$g_{tt} = -(1+h) \left(1 - \frac{2Mr}{\Sigma}\right), \quad (17a)$$

$$g_{t\phi} = -\frac{2aMr \sin^2 \theta}{\Sigma} (1+h), \quad (17b)$$

$$g_{\phi\phi} = \frac{\Lambda \sin^2 \theta}{\Sigma} + ha^2 \left(1 + \frac{2Mr}{\Sigma}\right) \sin^4 \theta, \quad (17c)$$

$$g_{rr} = \frac{\Sigma(1+h)}{\Delta + a^2 h \sin^2 \theta}, \quad (17d)$$

$$g_{\theta\theta} = \Sigma. \quad (17e)$$

using the functions

$$\Sigma = r^2 + a^2 \cos^2 \theta, \quad (18a)$$

$$h = \sum_{k=0}^{\infty} \left(\epsilon_{2k} + \epsilon_{2k+1} \frac{Mr}{\Sigma} \right) \left(\frac{M^2}{\Sigma} \right)^k, \quad (18b)$$

$$\Delta = r^2 + a^2 - 2Mr, \quad (18c)$$

$$\omega^2 = r^2 + a^2, \quad (18d)$$

$$\Lambda = \omega^4 - a^2 \Delta \sin^2 \theta. \quad (18e)$$

We do not go into detail on properties of geodesic motion in the Johannsen-Psaltis spacetime; for a summary, see [24]. Points on the Poincaré section given by the equatorial plane $\theta = \pi/2$, $\dot{\theta} > 0$ parametrized by r , p^r are used for recurrence analysis. In this system, points from the outermost orbits which reach near the tip of the main island of stability are highly concentrated in this region, with much lower densities at higher values

of r . This affects the RQA quantifiers and is therefore a good test case for the present LSTM networks.

Following [24], we choose the spacetime parameter values $a = 0.5M$, $\epsilon_3 = 0.3$, and $\epsilon_k = 0$ for any $k \neq 3$. For integrals of motion we choose the values $E = 0.95\mu$, $L_z = 2.85\mu M$. The initial conditions are taken along the $p^r = 0$ line on the Poincaré section in $r \in [6.36M, 6.43M]$ spaced at $0.001M$. This sweep of initial conditions includes the $\omega_r/\omega_\theta = 2/3$ orbital resonance.

3. Higher-dimensional example: 4D map

In a Hamiltonian system with 2 degrees of freedom, alternative methods exist which can detect resonances, such as the rotation curve and its estimation using the 2-dimensional Poincaré section. However, already in a system with 3 degrees of freedom, the Poincaré section becomes 4-dimensional and these simple methods are no longer applicable.

As a result, one of the goals of the method developed in this article is to allow detection of resonances in higher-dimensional systems. Since the recurrence plots and quantifiers are fairly universal measures of the system's properties, we apply the model trained on 2-dimensional data to 4-dimensional data generated by a map defined as [25, 26]

$$x_{n+1} = x_n - K \frac{\sin(x_n + y_n)}{(\cos(x_n + y_n) + \cos(z_n + t_n) + 4)^2}, \quad (19a)$$

$$y_{n+1} = y_n + x_n \quad \text{mod } 2\pi, \quad (19b)$$

$$z_{n+1} = x_n - K \frac{\sin(z_n + t_n)}{(\cos(x_n + y_n) + \cos(z_n + t_n) + 4)^2}, \quad (19c)$$

$$t_{n+1} = t_n + z_n \quad \text{mod } 2\pi. \quad (19d)$$

The x and z coordinates correspond to actions, and y and t angles in a 2-degree-of-freedom map, and K is a perturbation parameter (the standard notation would be ϵ [25], which would clash with the recurrence threshold in this work).

While the full structure of this map's phase space is difficult to understand, we can visualize the resonances in the space of the actions (corresponding to angular frequencies) x and z using the chaotic indicator APLE, defined as

$$\text{APLE} = \sup_{t_1 < t \leq T} \left(\frac{\log(\xi(t)/\xi(t_1))}{\log(t/t_1)} \right). \quad (20)$$

This expression converges to 1 or diverges when $\xi(t)$ is a linear or exponential function, respectively. Therefore 1 is frequently chosen as a threshold to distinguish regular from chaotic trajectories. The geography of resonances in the 4D map of Eq. (19) is shown in Fig. 5.

We use two sweeps of initial conditions along $x \in [0, 2\pi]$ at $z = 1.7$ and $z = 2$, respectively. The grid

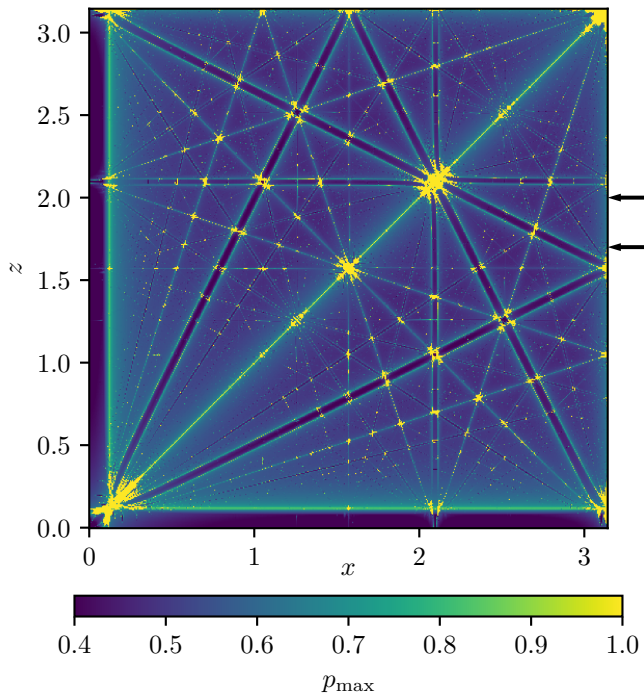


Figure 5. Geography of the resonances of the 4D map in the x, z plane. The arrows on the right side show the z values corresponding to the initial conditions taken in Figs. 9 and 10. The choice of the color mapping between 0.4 and 1 precludes us from identifying regular and chaotic trajectories individually; however, it clearly shows thin chaotic layers at the edges of resonances. The APLE is computed on a 501×501 grid and the perturbation parameter is set to $K = 0.05$.

along the x axis consists of 4001 samples with uniform spacing over the whole interval. All initial conditions satisfy $y = t = 0$. Following Fig. 5, the perturbation parameter is set to $K = 0.05$ in both cases.

III. RESULTS

We train the networks for 1000 epochs using the Adam optimizer [27] using a learning rate of $\eta = 10^{-5}$ and the PyTorch default values $\beta_1 = 0.9$, $\beta_2 = 0.999$, $\varepsilon = 10^{-8}$. The loss used for optimization is the mean squared error loss

$$\text{MSE} : \mathbb{R}^{mn} \times \mathbb{R}^{mn} \rightarrow \mathbb{R}, \quad (21a)$$

$$\bar{\mathbf{Y}}, \mathbf{Y} \mapsto \frac{1}{mn} \sum_{i=1}^m \sum_{j=1}^n (\bar{Y}_{ij} - Y_{ij})^2. \quad (21b)$$

Early experiments show that this produces much better results than using a binary cross entropy which seems the obvious choice for what is in principle a binary classification problem.

The network is trained on a grid of integer depths from 1 to 10 and dropout rates of 0, 0.1, 0.2, 0.3, and

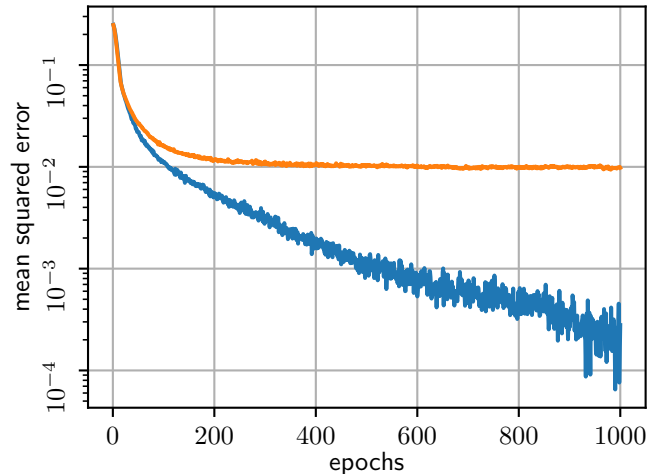


Figure 6. Evolution of the training (blue) and validation (orange) losses. Initial conditions are taken on the $y = 0$ line.

0.5. At each grid point, 4 independent networks are initialized and trained to prevent corruption due to insufficient sampling of the parameter space.

A. Basic network

The network which reached the lowest validation loss is one of the networks with 2 layers and dropout rate set to 0.5, its loss evolution is shown in Fig. 6.

1. de Vogeleare map

To demonstrate the effectiveness and robustness of the resonance detection network, we apply it to test data generated by a different system than the standard map. Fig. 7 shows the results of testing on the de Vogeleare map data. The perturbation parameter is set to $K = 0.56$ and 2001 initial conditions are used with linear spacing in $x \in [-0.44, 0.44]$ and $y = 0$. Initial conditions which lead to escaping trajectories are excluded on the basis of either coordinate's absolute value exceeding 10^4 at any point of the evolution.

All resonances in Fig. 7 are detected clearly by the network, with only few spurious jumps inside the main island of stability and in the chaotic zone on its right side. Besides these, the center of the main island of stability is also marked as a resonance.

2. Motion around a black hole

Fig. 8 shows the result of the basic network applied to the Poincaré section of a test particle following a geodesic in the Johannsen-Psaltis spacetime metric (see Sec. II F 2). The section contains a single resonance $\omega_r/\omega_\theta = 2/3$, which is detected by the network very

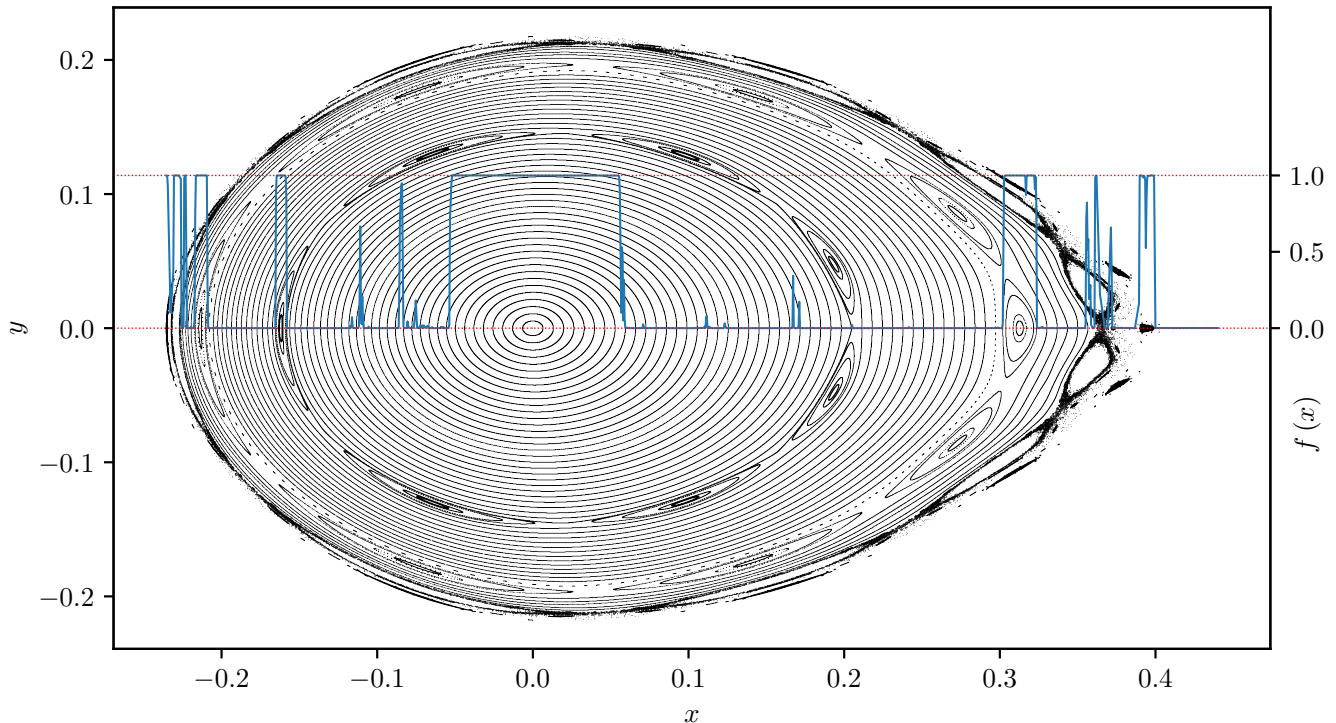


Figure 7. Results on the de Vogeleare map. The Poincaré section is shown in black, displaying several prominent resonances. The blue curve displays the outputs of the neural network from inputs based on initial conditions along the x axis with $y = 0$, the dotted red lines corresponding to the values 0 and 1 of the neural network output. While the network output is based on a total of 2001 initial conditions, the Poincaré section only uses 96 initial conditions to improve the clarity of the plot.

clearly. We note that while the figure shows surface of section points with initial starting at initial $r = 6.35M$ in order to fill out the top and bottom left corners of the plot, the network analyzes data starting at initial $r = 6.36M$.

3. 4D map

Finally, let us focus on the 4-dimensional map. Fig. 9 shows the output of the basic network over the two curves described in Sec. III F 3. For better orientation, the corresponding APLE curves are also shown.

In this case, no resonances are clearly recognizable in the network output.

B. Embedded network

While the full phase space contains more information than its reconstruction through embedding, there are cases where recurrence analysis may be more effective when applied to embedded data.

We train the same network architecture as the basic network with only one modification: the training recurrence quantifiers are recomputed based on the same original trajectories but only using the x coordinate with embedding. We use embedding dimension $m = 2$ and

time delay $\tau = 1$ for the embedded training data. These parameters have been determined using the false nearest neighbor algorithm and as minimum of the mutual information, respectively, on several trajectories representative of the dataset as a whole [28]. Again, the lowest validation loss is reached by one of the networks with 2 layers and a dropout rate of 0.5.

We perform the same experiment as in Fig. 9 using the embedded network. To compute recurrence quantifiers of the 4D map data, we use embedding with dimension $m = 4$ and time delay $\tau = 2$, set using the same algorithms as for the training data. Fig. 10 shows the results of the experiment. The classification is not as clear as, e.g., in the case of the 2D mapping (see Sec. III A 1). At the same time, the network is reacting to resonances in their true locations, albeit with variable heights of the output peaks as opposed to the 2D case.

We have also attempted to apply the embedded network to non-embedded 4D map data, as well as the basic network to embedded 4D map data. In both cases, the results were similar to those of Fig. 9 and no resonances were recognizable. Hence, the only combination that works is to use embedded network to embedded 4D map data.

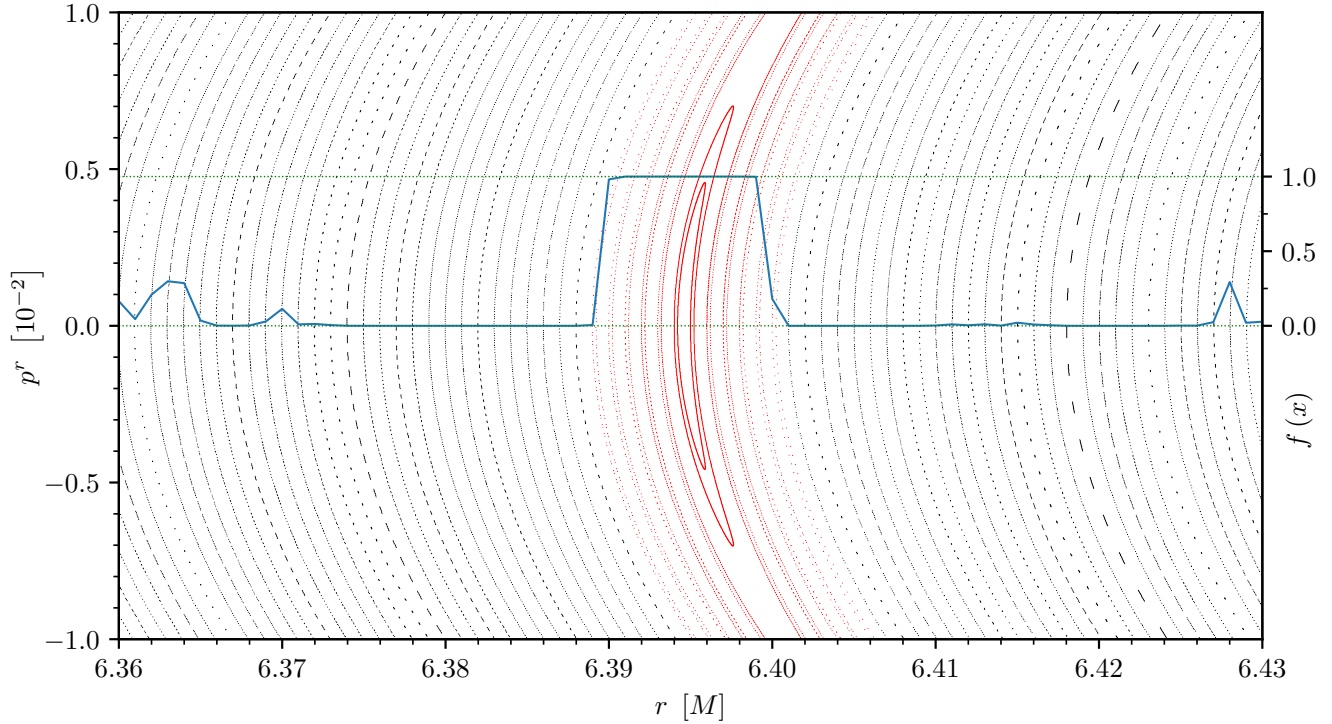


Figure 8. Results of the basic network on the Poincaré section of geodesic motion in the Johannsen-Psaltis spacetime superimposed on the corresponding Poincaré section. Shown in black and red are successive intersections of orbits corresponding to initial conditions along the $p^r = 0$ line with initial r between 6.35 and 6.43, spaced at 0.001. 10000 intersections are shown per initial condition, and the $1/3$ resonance is highlighted in red, while the KAM orbits are in black. The blue line shows the outputs of the neural network as a function of the initial condition along the $p^r = 0$ line, with green dotted lines showing the edge values of 0 and 1.

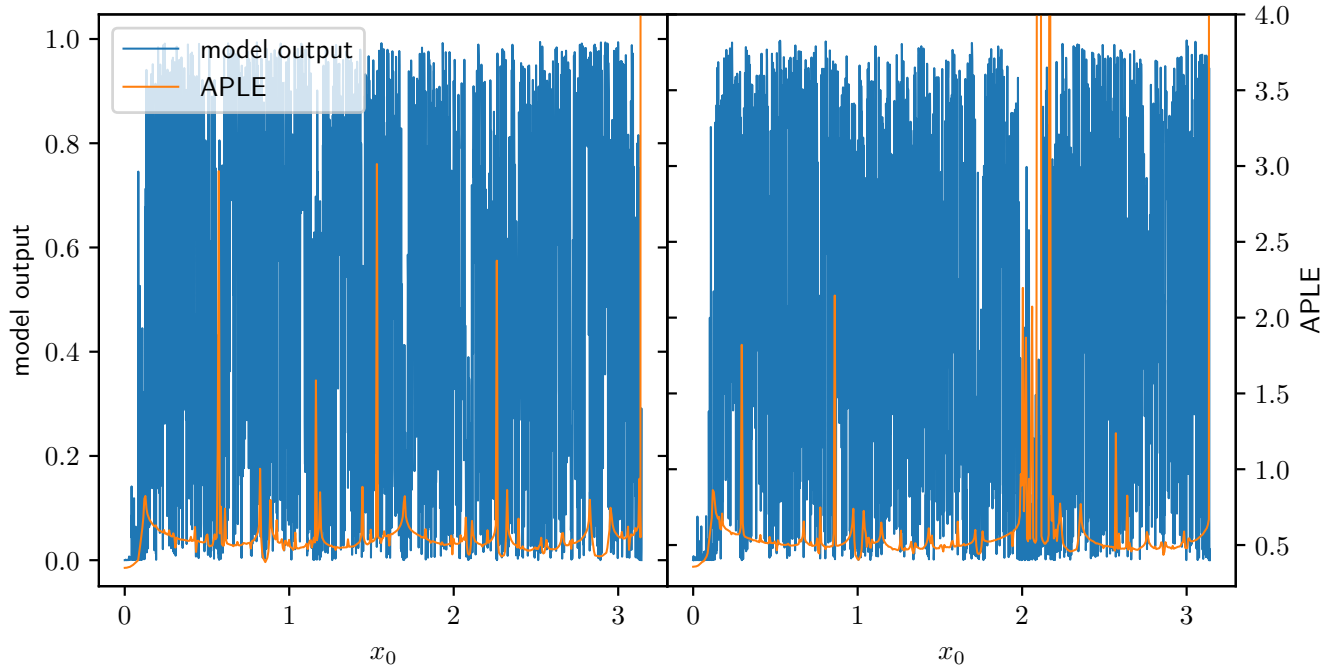


Figure 9. Results of the basic network on the 4D map. Each panel corresponds to 4001 initial conditions with $x_0 \in [0, \pi]$ and linear spacing, and $y_0 = t_0 = 0$. In the left panel, it holds $z_0 = 1.7$, and in the right, $z_0 = 2$. The primary y axis on the left corresponds to both model output curves, and the secondary y axis on the right corresponds to both APLE curves.

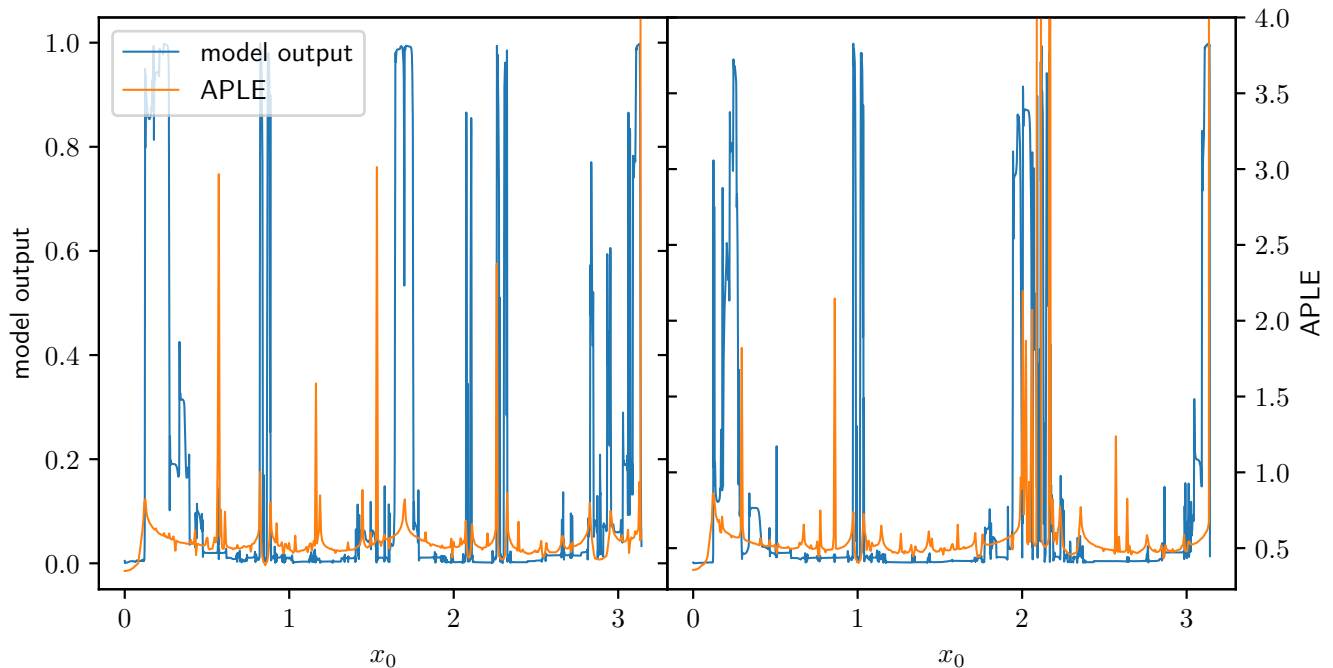


Figure 10. Results of the embedded network on the 4D map. Each panel corresponds to 4001 initial conditions with $x_0 \in [0, \pi]$ and linear spacing, and $y_0 = t_0 = 0$. In the left panel, it holds $z_0 = 1.7$, and in the right, $z_0 = 2$. The primary y axis on the left corresponds to both model output curves, and the secondary y axis on the right corresponds to both APLE curves.

IV. CONCLUSION

In this work, we have developed a machine-learning based method to uncover orbital resonances using recurrence quantification analysis (RQA) in dynamical maps. Using the Poincaré section method, applications to continuous-time data follow in a straightforward manner.

We have demonstrated the effectiveness of our algorithm on two primary test cases:

- the Poincaré section of a test particle near a perturbed black hole, as a model for the conservative portion of an EMRI, whose evolution is highly non-homogeneous in the phase space,
- a dynamical map in a 4-dimensional phase space, where the visualization tools which are critical for conventional methods are absent.

While the identification of resonances in the 4-dimensional case is not as clear as in 2-dimensional

cases, we conclude that this method is effective. Yet, there are multiple network parameters which can be optimized, along with engineering more general training data which may improve the performance of the method.

One of the primary motivations for this research is to identify orbital resonances due to the spin of the secondary in an EMRI. In this case, both issues above are relevant, as the general shape of the phase space remains similar in the orbital degrees of freedom, and another degree of freedom is added when the secondary gains a spin.

At the same time, Birkhoff chains arise generically in near-integrable systems, and appear in a large portion of problems in physics and related fields. As such, methods which aid in their detection and proper treatment are critical in many problems in physics and related fields.

V. ACKNOWLEDGMENTS

The authors are supported by the fellowship Lumina Quarentur No. LQ100032102 of the Czech Academy of Sciences.

[1] S. H. Strogatz, *Nonlinear Dynamics and Chaos*, 2nd ed. (CRC Press, London, England, 2019).
 [2] S. Mukherjee, O. Kopáček, and G. Lukes-Gerakopoulos, *Phys. Rev. D* **107**, 064005 (2023), arXiv:2206.10302 [gr-qc].

[3] O. Zelenka, G. Lukes-Gerakopoulos, V. Witzany, and O. Kopáček, *Phys. Rev. D* **101**, 024037 (2020).
 [4] P. Amaro-Seoane, *Living Reviews in Relativity* **21**, 4 (2018), arXiv:1205.5240 [astro-ph.CO].

- [5] P. Amaro-Seoane, J. Andrews, M. Arca Sedda, A. Askar, Q. Baghi, R. Balasov, I. Bartos, S. S. Bavera, J. Bellovary, C. P. L. Berry, E. Berti, S. Bianchi, L. Blecha, S. Blondin, T. Bogdanović, *et al.*, *Living Reviews in Relativity* **26**, 2 (2023), [arXiv:2203.06016 \[gr-qc\]](#).
- [6] G. Lukes-Gerakopoulos and V. Witzany, in *Handbook of Gravitational Wave Astronomy*, edited by C. Bambi, S. Katsanevas, and K. D. Kokkotas (2021) p. 42.
- [7] P. Suková and O. Semerák, *MNRAS* **436**, 978 (2013), [arXiv:1308.4306 \[gr-qc\]](#).
- [8] M. D. Hartl, *Phys. Rev. D* **67**, 024005 (2003), [arXiv:gr-qc/0210042 \[gr-qc\]](#).
- [9] N. Marwan, M. Carmen Romano, M. Thiel, and J. Kurths, *Physics Reports* **438**, 237 (2007).
- [10] T. Johannsen and D. Psaltis, *Phys. Rev. D* **83**, 124015 (2011), [arXiv:1105.3191 \[gr-qc\]](#).
- [11] A. N. Kolmogorov, *Doklady Akademii Nauk SSSR* **98**, 527 (1954).
- [12] V. I. Arnold, *Russian Mathematical Surveys* **18**, 9 (1963).
- [13] J. Moser, *Nachrichten der Akademie der Wissenschaften in Göttingen. II. Mathematisch-Physikalische Klasse*, 1 (1962).
- [14] G. D. Birkhoff, *Transactions of the American Mathematical Society* **14**, 14 (1913).
- [15] N. Marwan, *International Journal of Bifurcation and Chaos* **21**, 1003 (2011), [arXiv:1007.2215 \[nlin.CD\]](#).
- [16] G. Lukes-Gerakopoulos and O. Kopáček, *International Journal of Modern Physics D* **27**, 1850010 (2018), [arXiv:1709.08446 \[gr-qc\]](#).
- [17] O. Kopáček, V. Karas, J. Kovář, and Z. Stuchlík, *ApJ* **722**, 1240 (2010), [arXiv:1008.4650 \[astro-ph.HE\]](#).
- [18] F. Takens, in *Dynamical Systems and Turbulence, Warwick 1980*, edited by D. Rand and L.-S. Young (Springer Berlin Heidelberg, Berlin, Heidelberg, 1981) pp. 366–381.
- [19] S. Hochreiter and J. Schmidhuber, *Neural Computation* **9**, 1735 (1997), [https://direct.mit.edu/neco/article-pdf/9/8/1735/813796/neco.1997.9.8.1735.pdf](#).
- [20] R. Alfaidi and C. Messenger, (2024), [arXiv:2402.04589 \[gr-qc\]](#).
- [21] B. V. Chirikov, Research concerning the theory of nonlinear resonance and stochasticity (1971).
- [22] A. Morbidelli, *Modern celestial mechanics: aspects of solar system dynamics*, 1st ed. (CRC Press, 2002).
- [23] L. Reichl, *The Transition to Chaos: Conservative Classical Systems and Quantum Manifestations*, Institute for Nonlinear Science (Springer, 2004).
- [24] O. Zelenka and G. Lukes-Gerakopoulos, in *Workshop on Black Holes and Neutron Stars* (2017) [arXiv:1711.02442 \[gr-qc\]](#).
- [25] G. Lukes-Gerakopoulos, N. Voglis, and C. Efthymiopoulos, *Physica A: Statistical Mechanics and its Applications* **387**, 1907 (2008).
- [26] C. Froeschlé, M. Guzzo, and E. Lega, *Celestial Mechanics and Dynamical Astronomy* **92**, 243–255 (2005).
- [27] D. P. Kingma and J. Ba, in *3rd International Conference on Learning Representations, ICLR 2015, San Diego, CA, USA, May 7-9, 2015, Conference Track Proceedings*, edited by Y. Bengio and Y. LeCun (2015) [arXiv:1412.6980 \[cs.LG\]](#).
- [28] P. Suková, M. Grzedzielski, and A. Janiuk, *A&A* **586**, A143 (2016).
- [29] R. Hegger, H. Kantz, and T. Schreiber, *Chaos: An Interdisciplinary Journal of Nonlinear Science* **9**, 413 (1999), [https://pubs.aip.org/aip/cha/article-pdf/9/2/413/18301636/413.1_online.pdf](#).
- [30] N. Marwan, Commandline recurrence plots (2006), [https://tocsy.pik-potsdam.de/commandline-rp.php](#).
- [31] N. Marwan, Recurrence plots and cross recurrence plots (2024), [http://www.recurrence-plot.tk](#).

Appendix A: Codes

Code used to generate trajectories, train and evaluate the networks has been implemented in Python 3.11.5. The machine learning part has been done using the PyTorch framework version 2.1.0 through Python bindings. A release of the code used in this article is under preparation.

To determine optimal embedding parameters, the programs `mutual` and `false_nearest` from the TISEAN [29] package are used. All recurrence plots and quantifiers are computed using the commandline recurrence plots tool [9, 30, 31].